Acta metall. mater. Vol. 40, Suppl., pp. S161–S171, 1992
Printed in Great Britain.

0956-7151/92 $5.00 + 0.00

DIRECT MEASUREMENT OF LOCAL PROPERTIES OF INTERFACES WITH SCANNING TUNNELING MICROSCOPY

D. A. BONNELL, I. SOLOMON, G. S. ROHRER† and C. WARNER

The University of Pennsylvania, Department of Materials Science and Engineering, Philadelphia, PA 19104, U.S.A.

Abstract—Spatially localized measurements of structure and properties using scanning probe techniques (scanning tunneling microscopy, tunneling spectroscopy, local conductance profile measurement, etc.) have, for the most part, been restricted to single crystal surfaces. The application of these techniques to the study of atomic bonding at interfaces, of which at least one material is an oxide, is explored here in three model experiments. The intrinsic limit of spatial resolution of STM on low conductivity semiconductors (oxides) is first discussed. Then, the local density of states at a metal–TiO_2 interface is measured with tunneling spectroscopy and states associated with the metal–oxide bond identified. Local conductance profiles across individual grain boundaries in Si and $SrTiO_3$ are presented and space charge regions adjacent to oxide grain boundaries are directly detected. Finally, interface bonding is probed by characterizing topographic structure of gold–sapphire interface fracture surfaces.

Résumé—Des mesures spatialement localisées des structures et des propriétés utilisant les techniques de sonde en balayage (microscopie par effet tunnel, spectroscopie par effet tunnel, mesures du profil de conductance local etc.) ont, pour la plupart, été limitées à des surfaces monocristallines. L'application de ces techniques à l'étude de la liaison atomique aux interfaces—l'une d'entr'elles au moins étant un oxyde—est ici explorée dans trois expériences modèles. La limite intrinsèque de résolution spatiale de la microscopie à effet tunnel sur les semiconducteurs à faible conductivité (oxydes) est d'abord discutée. Puis, la densité locale d'états à l'interface métal/TiO_2 est mesurée par spectroscopie à effet tunnel et les états associés à la liaison métal/oxyde sont identifiés. Les profils de conductance locaux, à travers des joints de grains individuels dans Si et $SrTiO_3$, sont présentés et les régions de charge d'espace adjacentes aux joints de grains de l'oxyde sont directement détectées. Enfin, la liaison à l'interface est examinée en caractérisant la structure topographique des surfaces de rupture de l'interface or/saphir.

Zusammenfassung—Räumlich lokalisierte Messungen von Struktur und Eigenschaften mit Sonden-Verfahren (Rastertunnelmikroskopie, Tunnelspektroskopie, Messungen des lokalen Leitfähigkeitsprofiles usw.) waren meistens beschränkt auf einkristalline Oberflächen. In dieser Arbeit wird die Untersuchung der atomaren Bindung an Grenzflächen, bei denen mindestens ein Material ein Oxid ist, mit diesen Methoden anhand von drei Modellexperimenten geprüft. Die intrinsische Grenze der räumlichen Auflösung der STM auf schlect leitenden Halbleitern (Oxiden) wird zuerst diskutiert. Danach wird die lokale Zustandsdichte an der Metall/TiO_2-Grenzfläche mit Tunnelspektroskopie gemessen; die mit der Metall/Oxid-Bindung zusammenhängenden Zustände werden identifiziert. Lokale Leitfähigkeitsprofile, gemessen über einzelne Korngrenzen in Si und $SrRiO_3$, werden vorgelegt. Die Raumladungsbereiche in der Nähe der Oxid-Korngrenzen werden direkt nachgewiesen. Schließlich wird die Bindung über die Grenzfläche gemessen, indem die topografische Struktur von Bruchflächen entlang von Gold/Saphir-Grenzflächen charakterisiert wird.

1. INTRODUCTION

Structure–property correlations provide the basis for much of the current understanding of materials behavior. While advances in electron microscopy, X-ray and neutron diffraction allow structural characterization on scales ranging from millimeters to nanometers, the same range of characterization has not been possible of properties. Quantification of mechanical, electrical, optical and magnetic properties involves macroscopic measurements that average over large volumes of material, usually containing a variety of local structures such as isolated defects, grain boundaries, etc. In many cases the average response is most pertinent to materials optimization and processing development; however, a lack of structure–property correlations which distinguish contributions due to local structural variations hinders development of fundamental understanding of the behavior of materials.

The invention of the scanning tunneling microscope (STM) [1] yielded a technology that allows spatially localized measurements on the scale of nanometers. While, emphasis is usually placed upon atomic imaging, a variety of local properties can also

†Present address: Carnegie Mellon University, Pittsburgh, U.S.A.

be probed, often concurrent with imaging to allow immediate structure–property correlation. Although progress is being made in local measurement of electrical, thermal, magnetic, optical and mechanical properties, the potential for scanning probe technology has yet to be exploited in property measurement. This paper addresses the challenge of local property measurement at metal–ceramic interfaces using STM. The metal–ceramic combinations chosen for these experiments include those of interest to electronic ceramics, heterogeneous catalysis and structural composites. After a discussion of local property measurement and the intrinsic limit on spatial resolution for ceramics, results of three studies which address interface bonding are presented. The first focuses on initial bonding in metal–oxide interface formation and involves TiO_2. The second considers the effect of interface charge on electrical properties adjacent to interfaces, comparing Si and $SrTiO_3$ grain boundaries. The third demonstrates the use of topographic imaging as an indirect probe of the strength of metal–oxide interface bonds. Thus interface bond formation, properties near the interface, and properties at the interface are examined with scanning probe techniques.

2. LOCALIZED PROPERTY MEASUREMENT

The scanning technology of STM allows positioning of a local measurement probe; the property measured being limited only by the configuration of the probe and detection devices. Thus, the configuration referred to as the atomic force microscope (AFM) can be used to measure van der Waals interactions, electrostatic forces and magnetic properties. Modifications of the STM allow local density of states (tunneling spectroscopy), conductance, capacitance, work functions, photon emission, photon absorption, thermal gradients and, of course, surface topography to be probed [2]. This paper focuses on local density of states, conductance and topographic structure which are discussed in terms of application to metal–ceramic interfaces.

2.1. Local density of states

Early in the development of STM it was recognized theoretically [3] and experimentally [4] that current/voltage relationships measured across a *vacuum tunneling gap* are related to the density of states of the sample, provided that the electronic structure of the tip is a weak function of energy. The consequence of this relationship is that the current/voltage characteristics at the sample-tip junction, when differentiated and normalized, indicate the energies of local states from the valence to the conductance band edges, inclusive. The association of these states with bonding configurations is referred to as scanning tunneling spectroscopy. Many of the defects common in oxide structures, including oxygen vacancies, dopant defect states and splitting of nonbonding orbitals of transition metal elements, are in the energy range probed by tunneling spectroscopy.

Tunneling spectra are acquired by interrupting the image scan at a designated position, disabling the feedback circuit, and monitoring the current as the sample-tip bias is varied. Several spectra are averaged to increase the signal-to-noise ratio, with the feedback periodically enabled to avoid vertical drift during the measurement.

2.2. Conductance profiles

Conductance profiles are generated by extracting the values of current at a specified voltage from I/V curves acquired at different locations. This is, in effect, the instantaneous slope, dI/dV, one definition of conductance that can serve to characterize spatial variations in electrical properties. Conductance profiles from several voltages, at least one of each polarity, must be compared in order to characterize the change in rectification that often accompanies conductance variations. Since the space charge region under the tip often penetrates the sample, as is discussed in some detail below, the measurement contains a contribution from subsurface structure. For example, local number density of charge carriers can, in principle, be quantified by measuring capacitance at this junction. This requires simply varying the voltage ramp rate and monitoring the d.c. current which is an offset in the zero point of current.

2.3. Intrinsic limit on spatial resolution of ceramics

An important consideration in the application of STM to metal–ceramic interface analysis is the intrinsic limitation on spatial resolution due to limited sample conductivity. Spatial resolution is usually limited by tip condition and mechanical and electrical noise; however, an additional factor is critical in the case of low conductivity semiconductors (a description which includes many compounds considered ceramics). The usual assumption made in STM operation is that all of the voltage applied across the sample-tip junction is dropped within the vacuum. In low conductivity materials some of the voltage is dropped across the sample in a space charge region directly below the tip. The situation is depicted schematically in Fig. 1. In cases where minority charge carriers can be ignored, the size of the zero bias space charge region is related to materials parameters as

$$d = \sqrt{\frac{2\epsilon kT}{q^2 N}}$$

where q is the charge on an electron, ϵ is the sample permitivity, N is the number density of charge carriers, k is the Boltzman constant and T is temperature. (This equation serves as a first order approximation and is derived solving Poissons equation with a metal/semiconductor abrupt junction approximation.) Thus, as the local charge carrier concentration increases, the space charge dimension

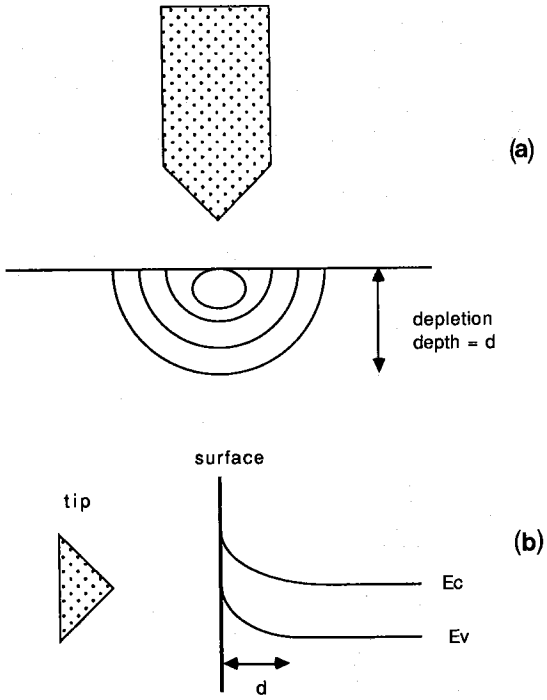

Fig. 1. Schematic describing space charge region under STM tip and associated band bending.

decreases. Strictly, the diameter of the space charge region is also proportional to the ratio of the carrier mobilities. Flores and Garcia [6] have shown that when minority carriers cannot be ignored the space charge diameter is also proportional to the ratio of electron and hole mobilities. The space charge diameter in silicon on which the 7×7 reconstruction is observed was calculated to be on the order of 2–5 Å. Calculations based on reasonable values of carrier concentrations and mobilities in ZnO predict space charge diameters ranging from 2 to 200 Å. The implication is that atomic resolution imaging should be possible on oxides with small space charge diameters, regardless of the fact that the energy bandgaps are >3.0 eV.

The spatial resolution of STM will be limited to some fraction of the radius of the space charge region (d from the equation above), since the space charge acts to smear out the details of local electronic structure. In addition, electrons near the Fermi energy must tunnel through the space charge region as well as the vacuum gap. Therefore, the minimum sample conductivity required for STM can be defined as that which results in the largest space charge through which electrons can tunnel. As the sample conductivity increases, the space charge region decreases with an accompanying increase in spatial resolution. The relationship between charge carrier concentration and spatial resolution has been observed experimentally in comparisons of tunneling behavior of oxides with similar energy bandgaps; TiO_2 and ZnO. In imaging crystallographic steps on polar and nonpolar faces of intrinsic ZnO single crystals with a number of various tips, the spatial resolution was consistently about 15 Å, as estimated by the smoothing of steps. However, atomic resolution was obtained on extrinsically doped ZnO. Similarly, reducing TiO_2, with the consequence of increasing the number of charge carriers in the sample and reducing the size of the space charge region, results in atomic scale resolution as shown in Fig. 2. It is important to note that, even in the cases of lowest spatial resolution, properties are measurable at unprecedented spatial scales.

2.4. *Description of experimental procedures*

STM analyses presented here were conducted on commercial† and "in-house" STM scanners controlled by "home made" feedback electronics and software of conventional design [7]. These systems allow the flexibility of interrupt feedback method of spectroscopy and property measurement. Mechanically formed Pt tips are "sharpened" *in situ* by applying a 90 V bias and passing 1 μA of current between the sample and tip for several minutes. The dependence of tunneling current on sample-tip separation is used to gauge the integrity of the vacuum gap when analysis is conducted in UHV. Confirmation of vacuum tunneling is absolutely necessary when interpreting spectra in terms of atomic structure, and is particularly critical in the analysis of oxides, during which sample-tip contact is common. Surface structure and chemistry are characterized with diffraction and Auger spectroscopy using a retarding field rear view LEED‡.

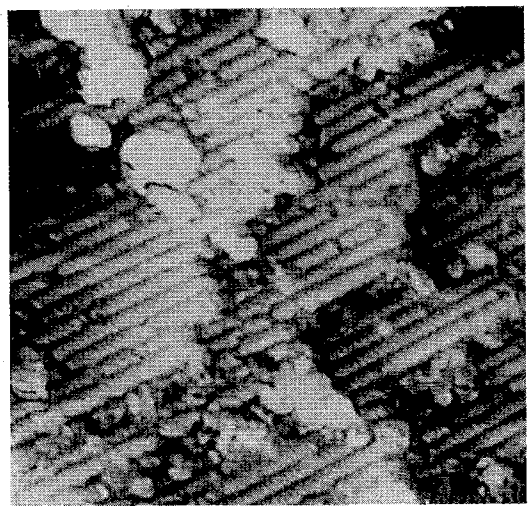

Fig. 2. Constant current STM image of a 246×246 Å area of TiO_2 (110) surface; $I = 0.1$ nA, $V = 2.0$ V. Large corrugations are aligned in the [111] direction with a period of 8.4 Å and corrugation height of 1.0 Å, while smaller corrugations along the rows have a period of 3.3 Å and amplitude of 0.2 Å.

†W.A. Technology.
‡Omicron.

3. LOCAL DENSITY OF STATES AT METAL–CERAMIC INTERFACES

Atomic bonding of a metal to an oxide will result in an alteration of the local electronic structure at and near the interface. The effect of bond formation may be limited to a small shift in the energy of atomic orbitals participating in the bond, or may be as dramatic as induction of defect states and/or significant charge transfer. The geometric positions of atoms and the local density of states at and near the interface reflect the character of interface bonding. The importance of the details of this interaction is such that much experimental effort (predominantly high resolution TEM analyses) and recent theoretical effort has been directed towards investigating the structure of metal–ceramic interfaces [8, 9]. As discussed above, tunneling spectroscopy allows a direct probe of local bonding that can be applied to interfaces. In this case titania is both a model multivalent oxide with which to study metal bonding and a interesting catalyst substrate.

The approach taken in analysis of bonding at the metal–TiO_2 interface is that standard in surface science, i.e. the surface is cleaned in vacuum below 10^{-9} torr (UHV), the chemistry verified by Auger electron spectroscopy, the structure determined by low energy electron diffraction (LEED), and then the sample is treated such that metal covers a fraction of the surface. A titania (110) surface was cut from a large single crystal and mechanically polished to 1 micron. The crystal was reduced in UHV by annealing in resistively heated tantalum boat at 800–1000°C for 36 h. The surface was then argon ion milled for 5 min at 2 KV followed by 25 min of ion bombardment at 500 V, the estimated current density being 5–10 μA/cm^2. The crystal was then annealed at 550°C for 30 min at 1×10^{-7} torr in order to oxidize the surface and anneal structural damage. LEED patterns indicate that this process produces a 1×1 bulk terminated surface.

In contrast to LEED, STM imaging revealed the presence of at least three periodic structures on the reduced TiO_2 (110) surface. An example is shown in the constant current image in Fig. 2, illustrating local structure not detected by the other surface analytical techniques. Fourier analysis and direct measurement of the image indicate that the rows oriented in the [111] direction have an 8.5 Å periodicity and a 1 Å corrugation height. The corrugation directed along the rows has a 3.3 Å periodicity with a corrugation height of 0.2 Å. Both the crystallography of the periodic structure and the heights of the features are consistent with accommodation of oxygen vacancies on (121) planes. This accommodation is accompanied by a shear displacement of $\frac{1}{2}$[110] resulting in steps as this structure intersects the surface. The development of this structure and two other variants are described in Refs [10] and [11]. In the bulk these crystallographic shear structures are referred to as Magneli phases.

The regions with high contrast, such as the one at the top left of Fig. 2, are adsorbates with metallic properties. Tunneling spectra typical of the periodic structure of the oxide and of the edges of the metallic "islands" where metal–oxide interactions might be observed are compared in Fig. 3. The electronic structures of the surfaces appear similar to the bulk structure, i.e. the valence band and the conduction band edges indicate a bandgap of about 3.2 eV. The defect state at about 0.5 eV below the conduction band edge is associated with oxygen vacancies. Although cluster calculations predict this energy to be 1.65 eV [12], the value measured by tunneling spectroscopy is consistent with experimental determination by photoemission [13]. The spectra for the edge of the "island" exhibit marked differences in electronic structure; specifically two additional states appear in the bandgap. Overlapping peaks 1.4 eV and 1.9 eV above the valence band edge, as shown in Fig. 3(b) result in a significant reduction in the apparent surface bandgap. Since these states are spatially localized to the vicinity of the island–oxide interface, they are indicative of the character of atomic bonding at these sites.

It is not yet possible to propose an atomic model for interactions between TiO_2 (110) and metallic species since the identity of the atoms in the islands

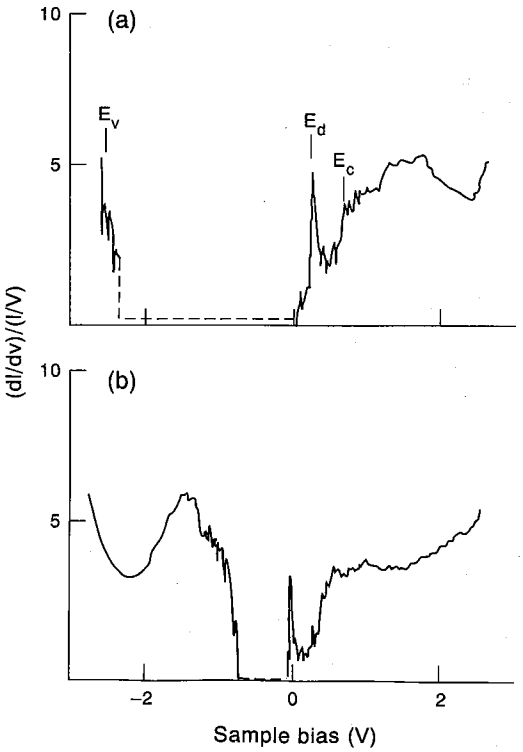

Fig. 3. Tunneling spectra from the TiO_2 structure, (a) from the oxide surface on which a state occurs 0.5 eV below the conduction band edge, and (b) from the edge of the metallic "island" at the top left of Fig. 2. Additional occupancy is observed 1.4 and 1.9 eV above the valence band edge.

has not been independently determined. Nevertheless, we can note several important preliminary conclusions. The surface energy gap persists even in the center of the metallic "islands" suggesting that at low coverages the islands retain some oxide character. The electronic structure at the island–oxide interface is different than that of the oxide or that of the metal exhibiting initial stages of metal–oxide interface formation. To the authors' knowledge, the results described here represent the first local measurement of electronic structure at a metal–oxide interface.

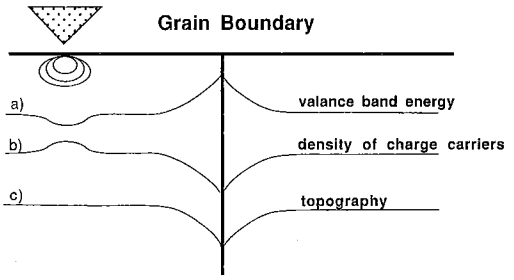

Fig. 4. Schematic of a grain boundary inducing a space charge within the adjacent grains intersecting a surface. Carriers trapped at the grain boundary cause a potential increase at the interface, charge neutrality requires a depletion zone adjacent to the boundary.

4. LOCAL CONDUCTANCE AT GRAIN BOUNDARIES

In the case of metal–oxide interfaces which are relevant to electronic ceramics, the charge state of the interface and induced variations in local electrical properties in the vicinity of the interface are critical consequences of interface bonding. The difficulty in appraising the relations experimentally is associated with the inability to make local property measurements at individual interfaces. In the first stage of examining this issue, attention is focussed on grain boundaries in polycrystalline semiconductors; specifically Si and $SrTiO_3$.

The approach taken in the analysis of grain boundary conductance is analogous in configuration to cross sectional TEM, i.e. the interface is perpendicular to the surface. The situation in the STM configuration is depicted in Fig. 4. The presence of the grain boundary at the surface is expected to result in a geometric feature, for example a depression due to thermal grooving or a step on a fractured surface. Superimposed upon this geometric structure will be a local perturbation of the band structure in response to local atomic disorder at the grain boundary. Additionally, variations in local charge carrier concentration may result from electrostatic forces due to trapped charge at the grain boundaries. The band energy profiles and the charge carrier profiles (which need not be independent) will depend on the type of defect at the interface, specifically whether it is an electron trap or a hole sink. Distinguishing the electronic variations from the geometric variations requires simultaneous imaging and measurement of conductance, a procedure which has been described in detail [7]. The notable result is that the charge carrier density profiles can be characterized if the lateral scale over which they exist is larger than the space charge region below the STM tip.

We compare here conductance profiles across silicon grain boundaries with those across more complex $SrTiO_3$ boundaries. In Fig. 5 transmission electron micrographs illustrating the morphology of a low pressure vapor deposited (LPCVD) silicon polycrystalline film are shown, along with STM images of the same material. While large grains are heavily twinned, small grains are apparently free from twins. The STM imaging indicated that the deposition process and subsequent etching produced a rough surface. Occasionally a grain could be identified which had clearly delineated boundaries, as does the one in Fig. 5. The grains analyzed by STM were always toward the small end of the grain size distribution; that is grain diameters range from 500 Å to 1.0 μm but STM analysis focussed on those smaller than 1000 Å. Current/voltage curves were acquired at 20–50 Å intervals across several boundaries. Typical tunneling spectra are shown, along with conductance profiles in Fig. 6. In every case the grain boundaries appeared more rectified and exhibited a higher conductance than did the grains. The region of higher conductance appeared to extend 10–20 Å into the grains; however, this dimension is on the order of the size of the tip which may be the limiting factor in this case. The change in conductance was observed regardless of the dopant species and is consistent with an increase in defects states associated with the disruption of order at the grain boundary.

In the case of oxides that have high dielectric constants and can accommodate nonstoichiometry, the disorder at the grain boundary results in an electrical potential barrier. This can be thought to arise from electrons trapped at undercoordinated atoms or segregated dopants. Charge neutrality requires that the regions immediately adjacent to this increased electron density be compensated by electron depletion. The configuration is illustrated in Fig. 7. The presence of space charge regions has been surmised based on segregation profiles of cations [14, 15] and macroscopic nonlinearity in electrical behavior, but has not, to our knowledge, been directly measured. The local conductance at such a space charge region could be detected by local measurements of conductance as shown schematically in Fig. 7. Within the grains the conductance will reflect the average electronic structure of the compound. At the boundary a higher conductance is expected due to local atomic disorder. Details of tunneling spectra from these regions may eventually lead to detailed information about the interface structure. In the space charge region a markedly different conductance is expected to reflect the electronic defects in this region.

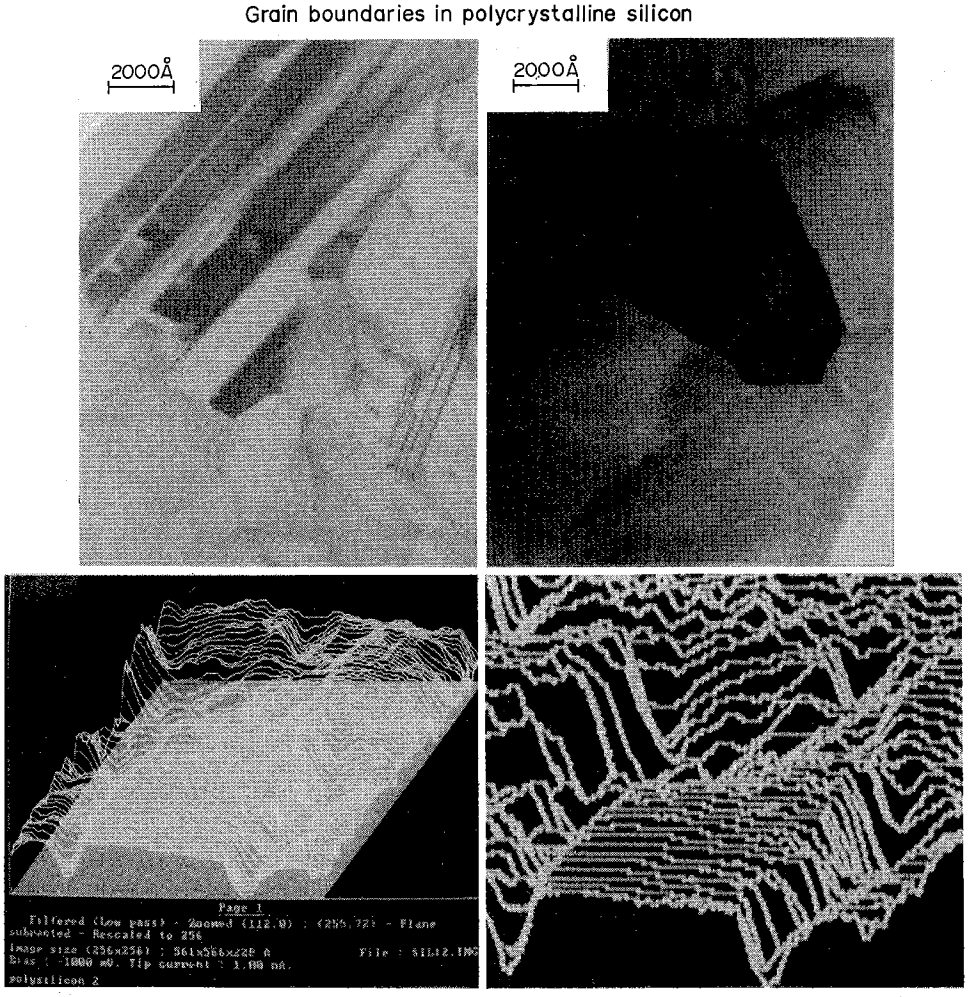

Fig. 5. The morphology of LPCVD polycrystalline silicon characterized by TEM is compared to surface morphology as characterized in constant current STM imaging. A small grain is shown around which the grain boundaries are clearly defined.

Polycrystalline samples were made from powders produced by decomposition of citrates, sintered in air at 1450°C for 1 h, and rapidly cooled [11]. Pellets were mechanically polished to $<0.5\,\mu$m and ultrasonically cleaned. Some samples were further reduced in a hydrogen anneal. Grain sizes ranged from 2.0 to 4.0 μm. Transmission electron microscopy indicated that most boundaries were free from secondary phases to within 15 Å. Tunneling spectra were acquired in UHV, after flashing the surface to desorb surface adsorbates, which, to within the detectability limit of Auger spectroscopy, eliminated carbon contamination.

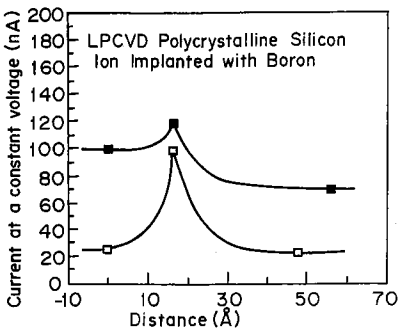

Fig. 6. Conductance profiles across two silicon grain boundaries, both located at 16 Å.

Polycrystalline samples doped with Cr and Nb were examined and all boundaries analyzed exhibited an increase in conductance similar to that observed in silicon. Spectra acquired across individual grains varied little, as shown in the conductance profile of Fig. 8. This consistency is remarkable given that the topography contains several surface features and that the measurement error is on the order of the size of the data points. The constant conductance implies a distribution of defects that is homogeneous on the spatial scale of the space charge under the tip; about 100 Å. Tunneling spectra from across a grain boundary are shown in Fig. 9, which also indicates the positions with respect to the grain boundary

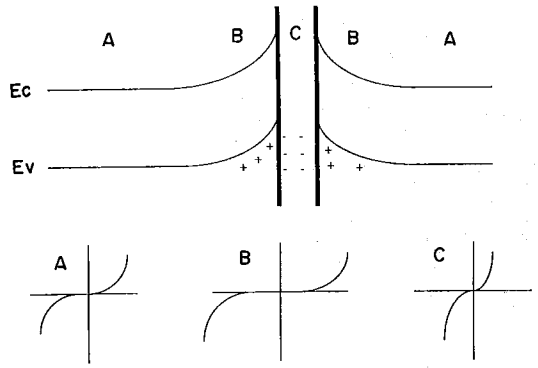

Fig. 7. Schematic of space charge region effect on tunneling. The simplified band diagram is used to indicate a boundary with negative interface charge, electron depletion adjacent to the boundary and the conductance characteristics expected in the grain (A), in the depletion region (B), and at the interface (C).

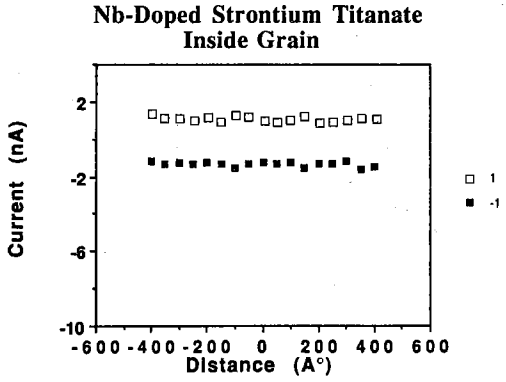

Fig. 8. Positive and negative polarity conductance profiles across a grain illustrating the constant conductance in spite of the presence of surface features.

at which the behavior changes. The conductance illustrated in 9(c) is observed on the left grain, that in 9(e) is observed on the right grain, and that in 9(d) is observed at the grain boundary.

In several cases a decrease in conductance was observed before the characteristic increase at the boundary. This result is illustrated in Fig. 10, which shows a conductance profile across a grain boundary that is on the extreme left of the plot. This local decrease in conductance, and associated increase in rectification, is much larger than any experimental error as can be seen by comparison with Fig. 9. The high conductance at negative polarity and zero conductance at positive polarity correspond to a negative grain boundary charge. Referring to the model of grain boundary space charge in Fig. 7,

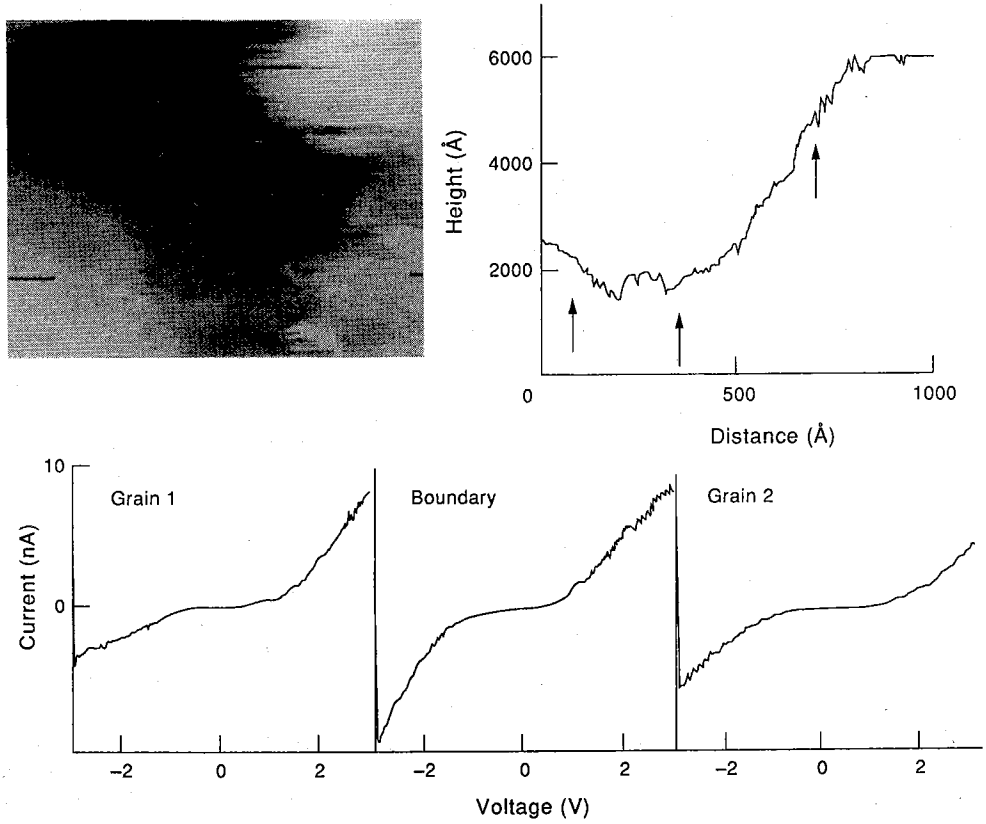

Fig. 9. Conductance of a $SrTiO_3$ grain boundary. The constant current grey scale image has a full scale (black to white) range of 4000 Å. A profile extracted from the image is shown to indicate the regions of various conductivity. The surface properties left of the first arrow, those right of the third arrow, and those at the depression representing the grain boundary are shown.

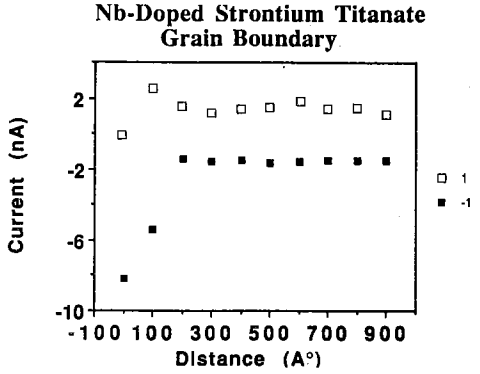

Fig. 10. Positive and negative conductance profiles from a region adjacent to a grain boundary, located at 0 Å, in polycrystalline $SrTiO_3$. Currents at 1.0 and −1.0 volts are compared. A large increase in conductance is observed at the grain boundary, but a decrease in conductance occurs immediately adjacent to the grain boundary.

the decreased conductance corresponds to region B. In this depletion region the density of carriers below the Fermi energy decreases, while that above the Fermi energy increases, consistent with conventional space charge theory. The size of the space charge region can be bounded by these observations to be between 20 and 160 Å. The lower bound is in agreement with equilibrium models of space charge which associate the range of its influence to the Debye length of solutes [16]. The upper bound is well within the range expected when oxides are annealed to enhance nonlinear electrical properties. In the latter case nonequilibrium states of off-stoichiometry are kinetically constrained in regions near the grain boundaries, supposedly allowing much larger space charge region to develop.

A comparison of the tunneling spectroscopy on silicon and strontium titanate grain boundaries illustrates both the capabilities and the limitations of grain boundary characterization. In high conductivity materials in which the grain boundary space charge is on the same order as that under the tip, only the grain and interface conductance can be probed. In contrast, it is possible to determine the sign of the interface charge, the spatial extent of the grain boundary space charge, and the character of the defects in the space charge region, in addition to the grain conductance in complex oxides.

5. LOCAL METAL–OXIDE BOND STRENGTH

One of the consequences of atomic bonding at metal–oxide interfaces is a resistance to interface separation, or fracture. In the case where a metal bonds directly to an oxide without forming a reaction product (or interphase) the energy required to separate the components is presumably related to the details of the bonding. If the composite can be separated exactly at the interface, the measured energy will be a consequence of the metal–oxide atomic bonding. The measured energy contains a contribution due solely to the metal–oxide bond strength and one due to any plastic dissipation in the metal [8]. The latter can be many times that of the former. Generally, when the atomic bond strength is low the interface fractures before high stresses can be developed. Conversely, when the atomic bond strength is high, stresses can locally exceed the value for dislocation generation in the metal. Evidence of plasticity should be manifest in the topographic structure of the metal fracture surface in a manner that can be quantified.

The criteria required to probe metal–oxide bond strength, e.g. the absence of interphase formation and the ability to fracture the interface, are met only in a few model systems. One such system was studied by Reimanis *et al.* [17] who have characterized the mechanical properties of the gold–sapphire interface and noted stress corrosion effects in ambient atmosphere. Topographical analysis of these fracture surfaces by STM yields a more microscopic characterization of the structure that complements the previous observations. Furthermore, since STM image data are stored digitally it is amenable to mathematical manipulation, as has been shown in the spectral analyses of fractal surfaces [18]. A variation of this procedure is applied to the analysis of the gold–sapphire interface fracture.

The topographic structure of the surface resulting from gold–sapphire interface fracture in air is compared to that resulting from fracture in dry nitrogen in Fig. 11. In these images the contrast indicates the height of the surface; i.e. the dark areas are low whereas the light areas are high. Both images are normalized to the largest features; therefore the total scale of vertical features in 11(a) is 6000 Å, while that in 11(b) is 1000 Å. Profiles extracted from each image are compared in 11(c–f). The largest features in the image of the air sample are on the order of 100 Å while those in the nitrogen sample are 500–1000 Å. Similarities of the microscopic features are not obvious when shown in the scales of Fig. 11, but can be compared in Fig. 12. Here profiles extracted from the images are shown on scales that allow comparison of the smaller features which are superimposed upon the larger features of both surfaces. On both surfaces this fine structure has lateral dimensions of about 100 Å and heights of 25-30 Å. On the sample fractured in nitrogen, the features appear elongated with aspect ratios of 3–5.

The difference in the sizes of the larger scale features is consistent with the measured fracture energies. When fractured in nitrogen the energy is increased by a factor of 5–6 over that measured during fracture in air [17]. The supposition is that chemical assistance in bond rupture lowers the effective atomic bond strength and, consequently, the amount of plasticity that is dissipated before fracture. The differences in size of the topographic features are of exactly this order. The relationship between

topographic structure and fracture energy can be examined with expressions developed by Evans *et al.* [19]

$$\Gamma = W_{ad}\left[1 + \frac{EW_{ad}}{\sigma_y^2 h} + \frac{EH^2}{LW_{ad}}\right]$$

where Γ is the fracture energy, E is the elastic modulus of the metal, σ_y the metal yield stress, h the metal thickness, H the amplitude and L the wavelength of the surface roughness, and W_{ad} the metal–oxide work of adhesion. The first term is characteristic of interface atomic bonding, the second represents the energy dissipated by plasticity, and the third represents the energy dissipated by friction. All three terms will be directly or indirectly affected by the strength of the interface bonds. The W_{ad},

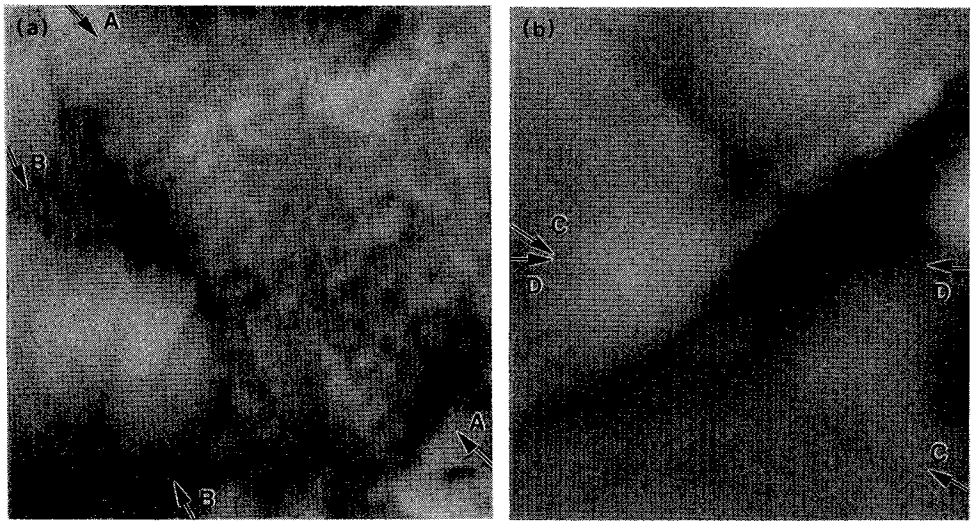

Fig. 11. Comparison of topographic structures of the metal side of the Au–sapphire interfaces fractured in air and under nitrogen. Constant current images were acquired with a current of 5 nA and bias of 400 mV. Full scale black to white in (a) is 6000 Å, in (b) is 1000 Å. Profiles extracted from the images of the surfaces quantifying the dimensions of the features.

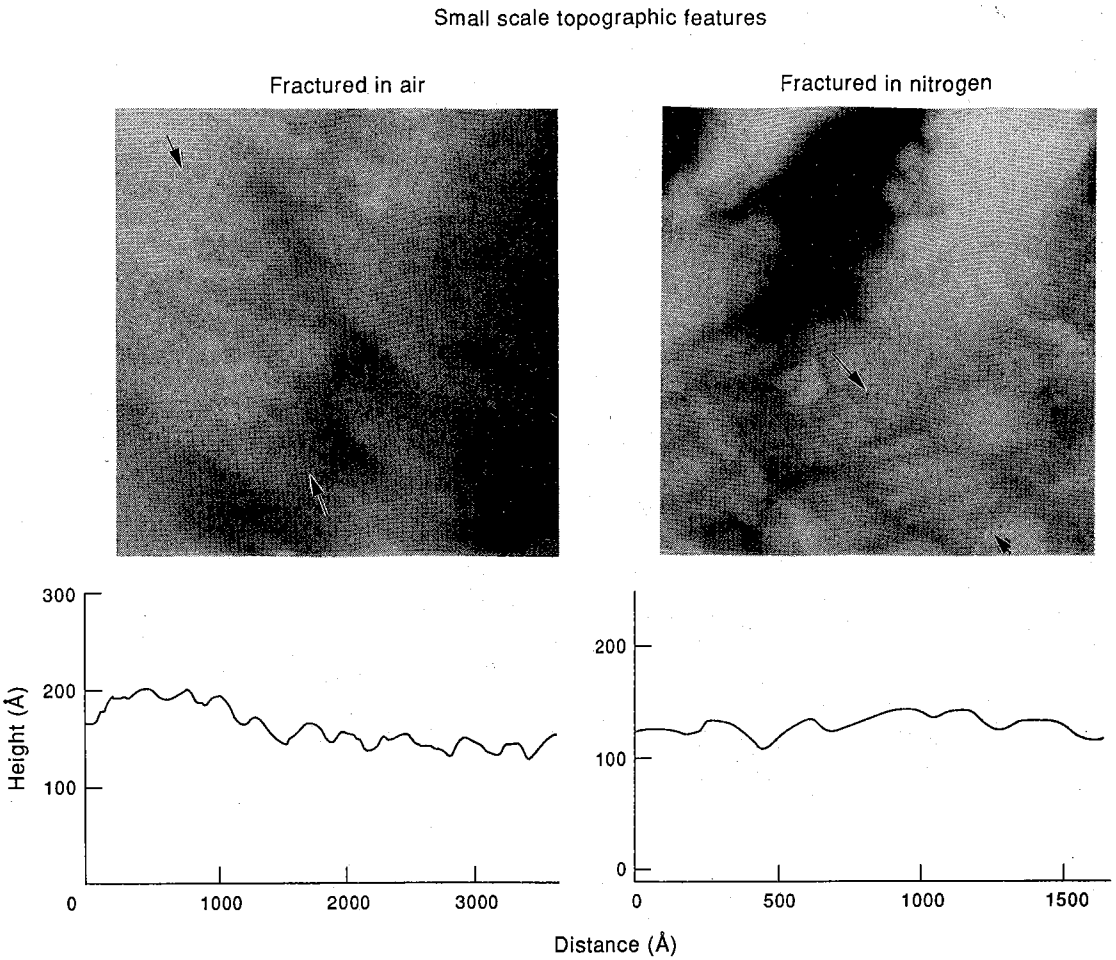

Fig. 12. Profiles extracted from both fracture surfaces emphasizing the microscopic details of the structure on the similar lateral scales.

usually on the order of 1–2 J/m^2, is so low that even a reduction as large as 50% from chemically assisted bond rupture will not cause the observed difference (50–200 J/m^2) in the magnitude of the fracture energy. The quantitative STM topographic measurements can be used to consider the relative contributions of the other two mechanisms of energy dissipation.

In considering the energy dissipated in plasticity, we note that in the regime of small scale yielding the energy release rate is proportional to the crack tip plastic zone size. The proportionality depends upon the modulus and yield stress of the materials and on constraints imposed on plastic flow by local loading and geometry. Thus, for a given metal–oxide interface in a specified test configuration, a factor of 5–6 decrease in the plastic zone size would be consistent with the observed decrease in the fracture energy. If the mechanism of plastic flow producing the surface features is linearly related to the plastic zone size, then the exact correlation between the size of these structures and fracture energy is not a coincidence and all of the energy difference is accounted for in the plasticity term. In the opposite limit, in which the measured surface roughness is assumed to contribute to fracture energy only through the frictional term, the contribution can be calculated as follows. From Fig. 11 the H and L are estimated for the sample fractured in nitrogen as 700 and 8000 Å and for the sample fractured in air as 100 and 2000 Å, respectively. Setting the plasticity term equal to 0 and evaluating the equation above results in a ratio of 5:61, or a reduction in the fracture energy by a factor of 12. This value is larger than the measured value for the samples, suggesting that the frictional contribution can, at most, be only partially responsible for the energy differences. The presence of surface roughness many times larger than the structural features of the original interface implies that a significant amount of plastic flow does occur and, therefore, that the measured fracture includes both contributions.

In spite of the large differences in topographic structure on the 100 Å scale, the structure on the 20–30 Å scale is similar, regardless of the chemical environment. The interfaces were fractured in a sample consisting of a metal foil sandwiched between

two sapphire blocks. In this configuration, constraints are such that the maximum stress occurs several metal foil thicknesses ahead of the crack tip, where local debonding can occur [20]. This local bond rupture would not be expected to be mediated by the atmosphere and would, therefore, be expected to progress via the same mechanism in both samples. These observations have indirectly probed atomic bonding at gold–sapphire interfaces by quantifying the effect of bond strength on fracture mechanisms.

6. CONCLUDING REMARKS

These model experiments have served to examine the potential of using scanning probe techniques to obtain quantitative information regarding properties of interfaces in which at least one material is an oxide. While there is no question concerning the impact of such measurements in general, applicability to oxides and to interface structure was not clear. Several obstacles have been overcome, including identification of limits of imaging and tunneling spectroscopy on low conductivity materials. In considering the three results presented here, the impact of local property measurement to interface structure–property correlation becomes clear. (This is not to minimize the importance of geometric structure which is taken as obvious.) Atomic bonding during various stages of interface formation can be elucidated by measuring the local density of states. The effects of interface structure on the properties immediately adjacent to the boundary can be probed if they result in a perturbation of electrical properties, for example local nonstoichiometry in a space charge region. The effects of bond strength on interface fracture can also be probed, but in a less direct manner. Although all three approaches cannot generally be used simultaneously on a wide range of materials combinations, they can be applied independently as demonstrated by the present results. These three model experiments of local properties at interfaces can serve as a basis from which systematic studies of interface bonding can be developed.

Acknowledgements—The authors are indebted to Y. M. Chiang, A. G. Evans V. Henrich and I. Reimanis for providing samples and for many stimulating discussions and to M. Nowakowski for the TEM analysis. The TiO_2 work was supported by National Science Foundation under the Presidential Young Investigators Program and the $SrTiO_3$ work under Department of Energy, Office of Basic Energy Sciences under contract No. FE-FG02-90ER-45428.

REFERENCES

1. G. Binnig and H. Rohrer, *Helv. phys. Acta* **55,** 726 (1982).
2. See examples in Proc. Int. Conf. on STM/STS (edited by R. Feenstra), *J. Vac. Sci. Tech.* **A8** (1989) and D. A. Bonnell, G. S. Rohrer and R. French, *J. Vac. Sci. Tech.* **B9,** 551 (1991) for photon emission and conductance.
3. J. Tersoff and D. Hamann, *Phys. Rev. B* **28,** 1544 (1983).
4. R. M. Tromp, R. J. Hamers and J. E. Demnth, *Phys. Rev. Lett.* **55,** 1303 (1985).
5. S. M. Sze, *Physics of Semiconductor Devices.* Wiley, New York (1981).
6. F. Flores and N. Garcia, *Phys. Rev. B* **30,** 2289 (1984).
7. G. S. Rohrer and D. A. Bonnell, *J. Am. Ceram. Soc.* **73,** 3026 (1990).
8. M. Ruhle and A. G. Evans, *J. Mater. Sci. Engng A* **107,** 187 (1989).
9. P. Blochl, G. P. Das, H. F. Fischmeister and U. Schonberger, *Acta/Scripta Metallurgica Conf. Proc.*, Vol. 4, pp. 9–14 (1989); A. J. Freeman, C. Li and C. L. Fu, *Acta/Scripta Metallurgica Conf. Proc.*, Vol. 4, pp. 2–8 (1989).
10. G. S. Rohrer, V. E. Henrich and D. A. Bonnell, *Science, N.Y.* **250,** 1239 (1990).
11. G. S. Rohrer, V. E. Henrich and D. A. Bonnell, *Surf. Sci.*, submitted.
12. S. Ellialtioglu and T. Wolfram, *Phys Rev. B* **18,** 4509 (1978).
13. V. Henrich, G. Dresselhaus and H. J. Zeiger, *Phys. Rev B* **17,** 4908 (1978).
14. J. A. Ikeda, Y. M. Chiana and B. D. Fabes, *J. Am. Ceram. Soc.* **73,** 1633 (1990).
15. S. B. Desa and D. A. Payne, *J. Am. Ceram. Soc.* **73,** 3391 (1990).
16. M. F. Yan, R. M. Cannon and H. K. Bowen, *J. appl. Phys.* **54,** 764 (1983).
17. I. E. Reimanis, B. J. Dalgleish, M. Brahy, M. Ruhle and A. G. Evans, *Acta metall. mater.* **38,** 2645 (1990).
18. M. Mitchell and D. A. Bonnell, *J. Mater. Res.* **5,** 2244 (1989).
19. A. G. Evans, M. Ruhle, B. J. Dalgleish and R G. Charalambides, *Metall. Trans.* **21A,** 2419 (1990).
20. A. G. Varias, Z. Suo and C. F. Shih, under review.